International Journal of Solids and Structures 213 (2021) 93–102

Contents lists available at ScienceDirect

International Journal of Solids and Structures

journal homepage: www.elsevier.com/locate/ijsolstr

Buckling of ultrastretchable kirigami metastructures for mechanical programmability and energy harvesting

Yafei Wang [a,1], Changguo Wang [a,b,1,*]

[a] National Key Laboratory of Science and Technology for National Defence on Advanced Composites in Special Environments, Harbin Institute of Technology, Harbin 150001, PR China
[b] Center for Composite Materials, Harbin Institute of Technology, Harbin 150001, PR China

ARTICLE INFO

Article history:
Received 20 July 2020
Received in revised form 25 November 2020
Accepted 28 December 2020
Available online 31 December 2020

Keywords:
Buckling
Kirigami
Flexibility
Stretchability
Programmability
Energy harvesting

ABSTRACT

Metastructures based on kirigami (the Japanese art of paper folding and cutting) have great potential for applications in stretchable electronics, bioprobes, and controllable optical and thermal devices. However, a theoretical framework for understanding the physics of their buckling behavior and to facilitate the search for ultrahigh stretchability has yet to be developed. Here, we present such a framework based on an energy approach. Closed-form analytical solutions and scaling laws are obtained for some key mechanical quantities, including flexibility, normalized flexibility, critical buckling strain, maximum tensile strain, elastic stretchability, normalized stretchability, and out-of-plane stiffness. Both experiments and numerical calculations are performed to validate the accuracy and scalability of the theoretical model. Systematic analyses of key mechanical quantities reveal how it is possible to bridge the gap between kirigami design by experience and by mechanically guided design, as well as how various dimensionless geometric parameters can be used to regulate buckling responses. Illustrative applications show that the ability to predict and tune the mechanical programmability of the proposed theoretical framework enables stable electromechanical conversion and programmable electromechanical kirigami with domino-like buckling. This work provides a foundation for further research and can also aid in the design of kirigami for use in programmable metastructures and metamaterials and energy harvesting.

1. Introduction

Mechanically guided design of architected structures provides them with many exceptional properties ranging from ultrahigh specific stiffness, strength, and toughness (Bauer et al., 2016; Berger et al., 2017; Zheng et al., 2016) to three-dimensional (3D) topological reconfiguration (Overvelde et al., 2017; Zhang et al., 2017). Recently, kirigami, the Japanese art of paper folding and cutting, has attracted considerable attention as a superior design paradigm for the realization of engineered elasticity (Callens and Zadpoor, 2018). A key merit of buckling-induced kirigami metastructures is that they can be conveniently excised at specific locations when in their 2D state (An et al., 2019), after which local elastic instability (Rafsanjani and Bertoldi, 2017) can be exploited to transform them into multipotent 3D configurations under stretching (Babaee et al., 2020; Blees et al., 2015; Choi et al., 2019; Guan et al., 2018a, 2018b; Lamoureux et al., 2015; Rafsanjani et al., 2019, 2018; Tang et al., 2017; Yang et al., 2018) (see SI Appendix, Note 1). Furthermore, the incorporation of variable geometric design into kirigami metastructures creates new opportunities for enhancing their functions (Chen et al., 2018; Coulais, 2016; Dias et al., 2017; Florijn et al., 2014; Jin et al., 2019; Mortazavi et al., 2017), since it allows higher stretchability and lower stiffness (Wang et al., 2020). However, understanding the underlying relations between buckling properties (including flexibility, critical buckling strain, stretchability, and deformation response) and geometries requires the development of a theoretical framework for both nonbuckling and buckling kirigami metastructures with various thickness. Although some theoretical models (Wang and Wang, 2020; Wang et al., 2020) have been established for variable-geometry kirigami with the aim of analyzing the stiffness and stretchability using the theory of elasticity, they focus on in-plane deformation of thick kirigami and thus fail to predict the nonlinear properties of buckling kirigami.

This describes the development of a theoretical framework for kirigami metastructures undergoing stretching, as validated by

* Corresponding author at: National Key Laboratory of Science and Technology for National Defence on Advanced Composites in Special Environments, Harbin Institute of Technology, Harbin 150001, PR China.
E-mail address: wangcg@hit.edu.cn (C. Wang).
[1] These authors contributed equally to this work

https://doi.org/10.1016/j.ijsolstr.2020.12.018
0020-7683/

experimental data, an energy approach, and numerical simulation, and taking into account the effects of three typical motifs (referred to as Kirigami-1, Kirigami-2, and Kirigami-3). This framework is intended to provide a design principle for optimizing the flexibility, normalized flexibility, critical buckling strain, maximum tensile strain, elastic stretchability, normalized stretchability, and out-of-plane stiffness of kirigami metastructures. The accuracy and scalability of the theoretical framework are verified by 3D printing of fluorescent polymer-based kirigami and the measurement of out-of-plane mechanical properties of the kirigami surface. Systematic investigations and quantitative comparisons of nonlinear effects on prebuckling response, critical buckling strain, postbuckling behavior, and detailed deformation are performed via experiments, theoretical analyses, and finite element method (FEM) numerical simulations to shed light on the crucial roles of dimensionless geometric parameters, especially the long-arm effect. Furthermore, a novel design strategy associated with hybrid kirigami structures shows that the models developed here can be used to map simultaneous buckling to domino-like buckling, as well as to enable electromechanical programmability and stable device performance of ultrastretchable polyvinylidene difluoride (PVDF) kirigami.

2. Design strategy and energy approach to kirigami metastructures

Fig. 1 presents typical designs and deterministic buckling modes of kirigami metastructures. Simulations and the experiment methods are described in SI Appendix, Notes 13 and 14, respectively. Microscopic constructions based on these kirigami metastructures can be fabricated by a variety of manufacturing techniques, such as laser cutting, 3D printing, thin-film etching, and photolithography. The examples shown in Figs. 1–3 and Fig. 4 (except for 4 m) were formed using laser cutting, whereas those in Fig. 4m were formed by 3D printing.

To develop a strategy for expanding the design space of kirigami metastructures, we consider three such metastructures, namely, Kirigami-1, Kirigami-2, and Kirigami-3 (illustrated schematically in Fig. 1a), which are based on a schematic of the three kirigami designs described in detail in SI Appendix, Fig. S2. In particular, the microstructure in Kirigami-3 contains a curvature feature that can be characterized in terms of large-curvature curved beam (LCCB) theory, according to which the pure bending normal stress of the curved beam exhibits a hyperbolic variation along its cross section. Schematics of the three kirigami designs with their geometric parameters (ribbon width ω, arc radius R, connection length n, and thickness t, as well as the length l and width m of the tailored vacancy) are provided in SI Appendix, Fig. S2. These reduce to Kirigami-1, Kirigami-2, and Kirigami-3 when $2n = m = \omega$ without application of LCCB, when $2n = m$ without application of LCCB, and when $n = R$ with $m = 0$, respectively. Moreover, the kirigami metastructures and their buckling behaviors are also characterized by four independent dimensionless parameters, namely, the thickness-to-width ratio $\alpha = t/\omega$, the length-to-width ratio $\beta = l/\omega$, the spacing-to-width ratio $\gamma = m/\omega$, and the arc-radius-to-width ratio $\eta = R/\omega$, as well as the number of unit cells s.

The bucking mode of a kirigami metastructure is defined as antisymmetric or symmetric depending on whether the buckling morphology of the unit cell in the kirigami is respectively antisymmetric or symmetric about its transverse axis. Fig. 1b and 1c present experimental images of deformed kirigami (Kirigami-1 with $\alpha = 1/50$ and $\beta = 3$) illustrating representative buckling modes (i.e., antisymmetric and symmetric modes) and demonstrating the existence of two local energetic minima. To better understand the physics of buckling in such stretchable metastructures, we construct a theoretical framework and determine the scaling laws for the initial in-plane elastic response, the transition from in-plane to out-of-plane response, and the limits of the elastic response (for details, see SI Appendix, Notes 1–8). For the antisymmetric buckling mode, a sinusoidal deformation pattern of the beams can be observed experimentally (Fig. 1b). Therefore, the unit cell can be divided into two sinusoidal parts, and only the top beam needs investigated owing to the antisymmetric geometry. Here, the out-of-plane buckling deflection δ and out-of-plane buckling torsion angle φ can be chosen to describe the deformation, and they can be given in terms of sinusoidal functions as follows:

$$\delta = \delta_{as}\cos\varphi_a \sin(2\pi x/l)/2, 0 \leqslant x \leqslant l \tag{1}$$

$$\varphi = \varphi_a \sin(2\pi x/l), 0 \leqslant x \leqslant l \tag{2}$$

where δ_{as} is the out-of-plane deflection and φ_a is the amplitude of the torsion angle. The total potential energy in the unit cell is then given by $\Pi_A = U_{B-A} + U_{T-A} - W_{E-A}$, where U_{B-A} is the total elastic strain energy induced by bending deformation, U_{T-A} is the total elastic strain energy from torsion deformation, and W_{E-A} represents the work done owing to the external load. According to the principle of virtual work, the critical buckling force of the antisymmetric buckling kirigami can be determined by minimizing this total potential energy with respect to δ_{as} and φ_a, i.e., by solving $\partial\Pi_A/\partial\delta_{as} = 0$ and $\partial\Pi_A/\partial\varphi_a = 0$.

For the symmetric buckling mode (Fig. 1c), four sinusoidal beams and one opposite-sense bending shell can be used to characterize the deformation of the unit cell. According to Eqs. (1) and (2), the deflection δ and torsion angle φ of the top beam can be calculated using the following relations:

$$\delta = \delta_{\max}\sin(2\pi x/l), 0 \leqslant x \leqslant l \tag{3}$$

$$\varphi = \varphi_{\max}\sin(2\pi x/l), 0 \leqslant x \leqslant l \tag{4}$$

where $\delta_{\max}$ and $\varphi_{\max}$ are the maximum out-of-plane deflection and maximum torsion angle, respectively. Furthermore, the opposite-sense bending shell is a cylindrical shell, and so, according to the theory of plates and shells, its elastic strain energy generated by the opposite-sense deformation is given by $U_{S-S} = \frac{R_s r \Psi\theta}{2}(\Delta\kappa_x, \Delta\kappa_y)(M_x, M_y)^{\mathrm{T}}$ (for details, see SI Appendix, Note 5), where $\Delta\kappa_x = 1/r$ and $\Delta\kappa_y = 1/R_s$ are the variations in curvature along the transverse and longitudinal principal directions, respectively (see Fig. 1c), and M_x and M_y are the driving moments of the opposite-sense bending shell (Wang and Wang, 2018). The total potential energy of the symmetric buckling mode in the unit cell is given by $\Pi_S = U_{B-S} + U_{T-S} - W_{E-S} + U_{S-S}$, where U_{B-S} is the total bending energy of the sinusoidal beam, U_{T-S} is the total torsion energy, and W_{E-S} is the total work done by the external loading. The critical buckling force of the symmetric buckling mode can again be obtained by minimizing the total potential energy with respect to $\delta_{\max}$ and $\varphi_{\max}$: $\partial\Pi_S/\partial\delta_{\max} = 0$ and $\partial\Pi_S/\partial\varphi_{\max} = 0$.

3. Initial in-plane response and onset of buckling

The stress–strain curve in Fig. S1c (see stage I in SI Appendix, Note 1) shows that the response of an ultrastretchable kirigami metastructure is initially linear. In-plane deformation can guarantee an initial stiff regime. To obtain insight into geometry-dependent effects involving large curvature of kirigami metastructures, closed-form analytical results for prebuckling mechanical quantities are first derived using LCCB theory, Castigliano's theorem, and the Moore integral method, as detailed in SI Appendix, Note 2. The flexibility and normalized flexibility are particularly important mechanical indices. The flexibility is defined as the ratio between the effective displacement $2\delta_y$ and the external loading F

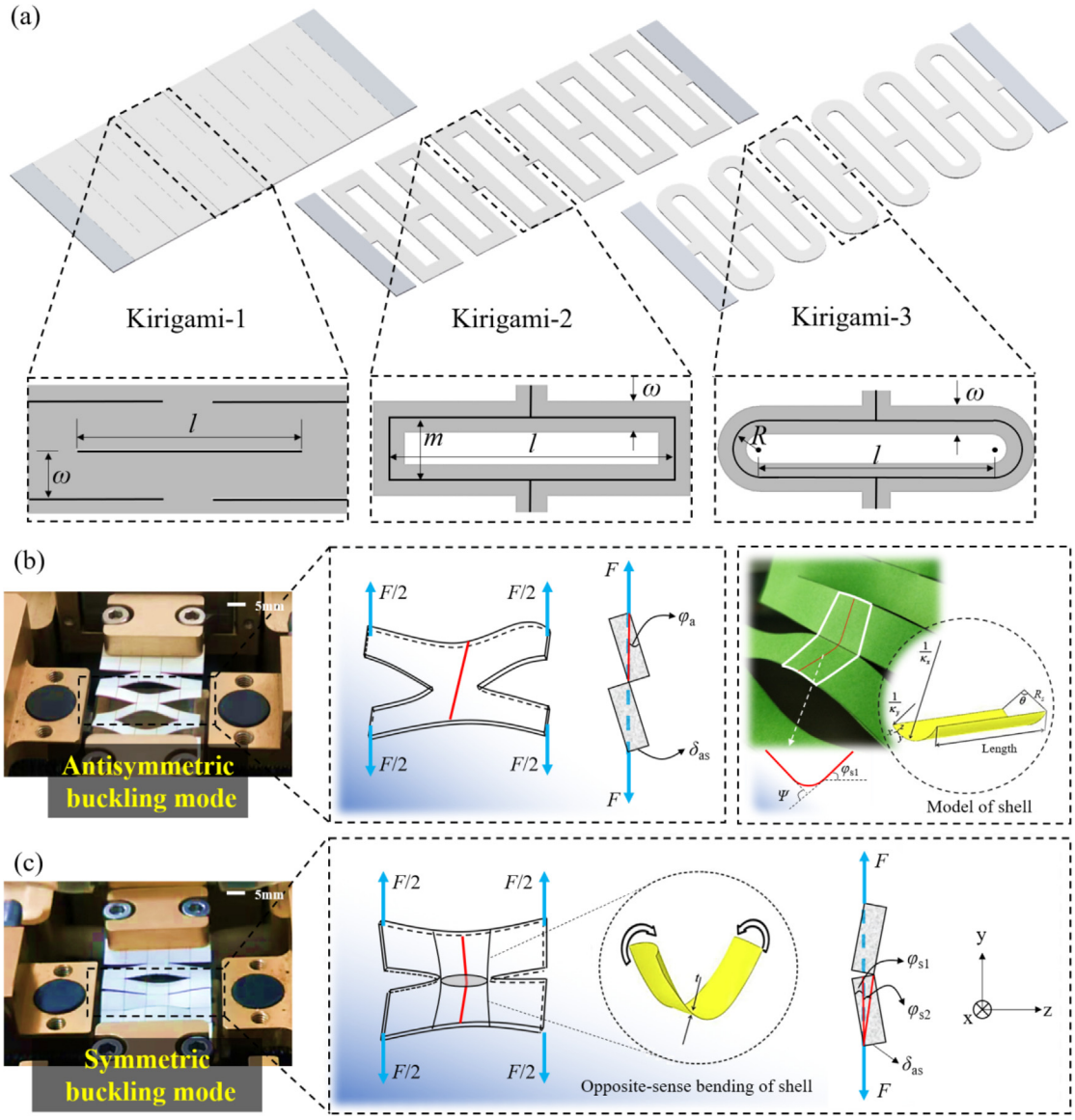

Fig. 1. (a) Schematics of kirigami metastructures together with their geometric parameters (width ω, length of arm l, spacing length m, arc radius R, thickness t, and number of unit cells s): Kirigami-1 (left), Kirigami-2 (middle), and Kirigami-3 (right). (b) Experimental image of the antisymmetric buckling mode of the kirigami metastructure under stretching. The metastructure can be described in a simplified manner in terms of a sinusoidal beam pattern and an antisymmetric geometry (with the out-of-plane deflection δ_{as} and torsion angle φ_a). (c) Illustration of the symmetric buckling mode of the kirigami from experimental observation. Based on the symmetric geometry (with out-of-plane deflection δ_{as} and torsion angles φ_{s1} and φ_{s2}) and the features of the deformation, the behavior of the kirigami unit cell under stretching can be characterized in terms of four sinusoidal beams and one opposite-sense bending shell with certain geometric parameters, namely, the curvatures κ_x and κ_y along the transverse and longitudinal principal directions and the central angle θ of the cylindrical shell with radius R_s.

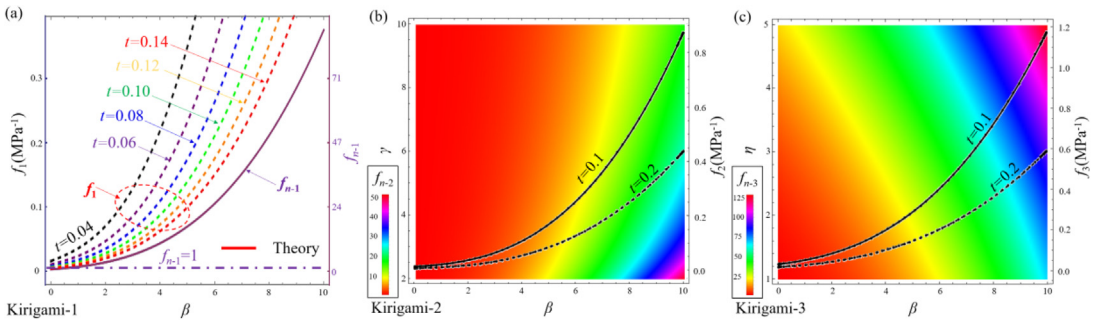

Fig. 2. Effects of geometric parameters ($t = \alpha\omega$, β, γ, and η) on flexibility and normalized flexibility obtained using LCCB theory for ultrastretchable metastructures of (a) Kirigami-1, (b) Kirigami-2, and (c) Kirigami-3.

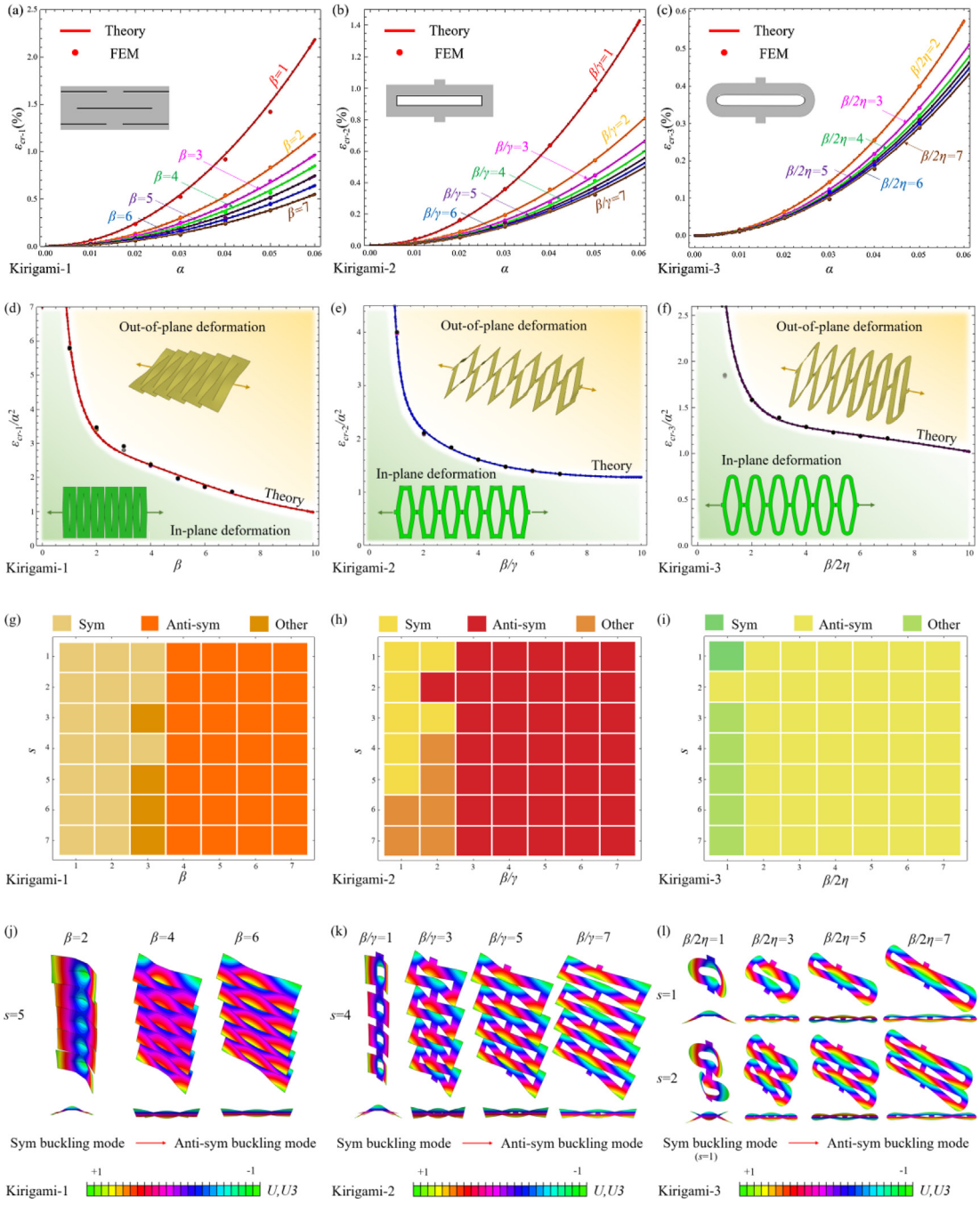

Fig. 3. (a–c) Effects of α on the critical buckling strain for Kirigami-1, Kirigami-2, and Kirigami-3, respectively, for different values of the geometric parameters β, β/γ, $\beta/2\eta$, and s. (d–f) Ratio of critical buckling strain to α^2 versus β in Kirigami-1, β/γ in Kirigami-2, and $\beta/2\eta$ in Kirigami-3, respectively, for various values of s (the unit cell number). (g–i) Phase diagrams obtained from numerical calculations demonstrating the variations in buckling configurations of Kirigami-1, Kirigami-2, and Kirigami-3, respectively, as the values of s and the geometric parameters β, β/γ, and $\beta/2\eta$ are varied. (j–l) Numerical snapshots of kirigami metastructures for Kirigami-1, Kirigami-2, and Kirigami-3, respectively, at the critical buckling strain, where the color bars represent the out-of-plane displacement U_3.

and can be calculated as $f_i = 2\delta_y/F$, where $i = 1, 2, 3$ can represent the Kirigami-1, Kirigami-2, and Kirigami-3 configurations. The flexibility of a defect-free straight ribbon of length $m + 2R + 2n$ (i.e., the unit cell length of the kirigami metastructure) and cross-sectional area A is given by $(m + 2R + 2n)/(EA)$, where E is Young's modulus and v is Poisson's ratio. Therefore, the normalized flexibility (i.e., the effective flexibility of the kirigami metastructure normalized by that of a defect-free straight ribbon of the same end-to-end length in the unit cell) can be calculated as $f_{n-i} = 2EA\delta_y/F(m + 2R + 2n)$. Through the energy approach, the flexibility and normalized flexibility are calculated in terms of the geometric parameters using the following relationships:

$$f_1 = f_1(t, \beta, E, v) \tag{5}$$

$$f_2 = f_2(t, \beta, \gamma, E, v) \tag{6}$$

$$f_3 = f_3(t, \beta, \eta, j(\eta), E, v) \tag{7}$$

$$f_{n-1} = f_{n-1}(\beta, v) \tag{8}$$

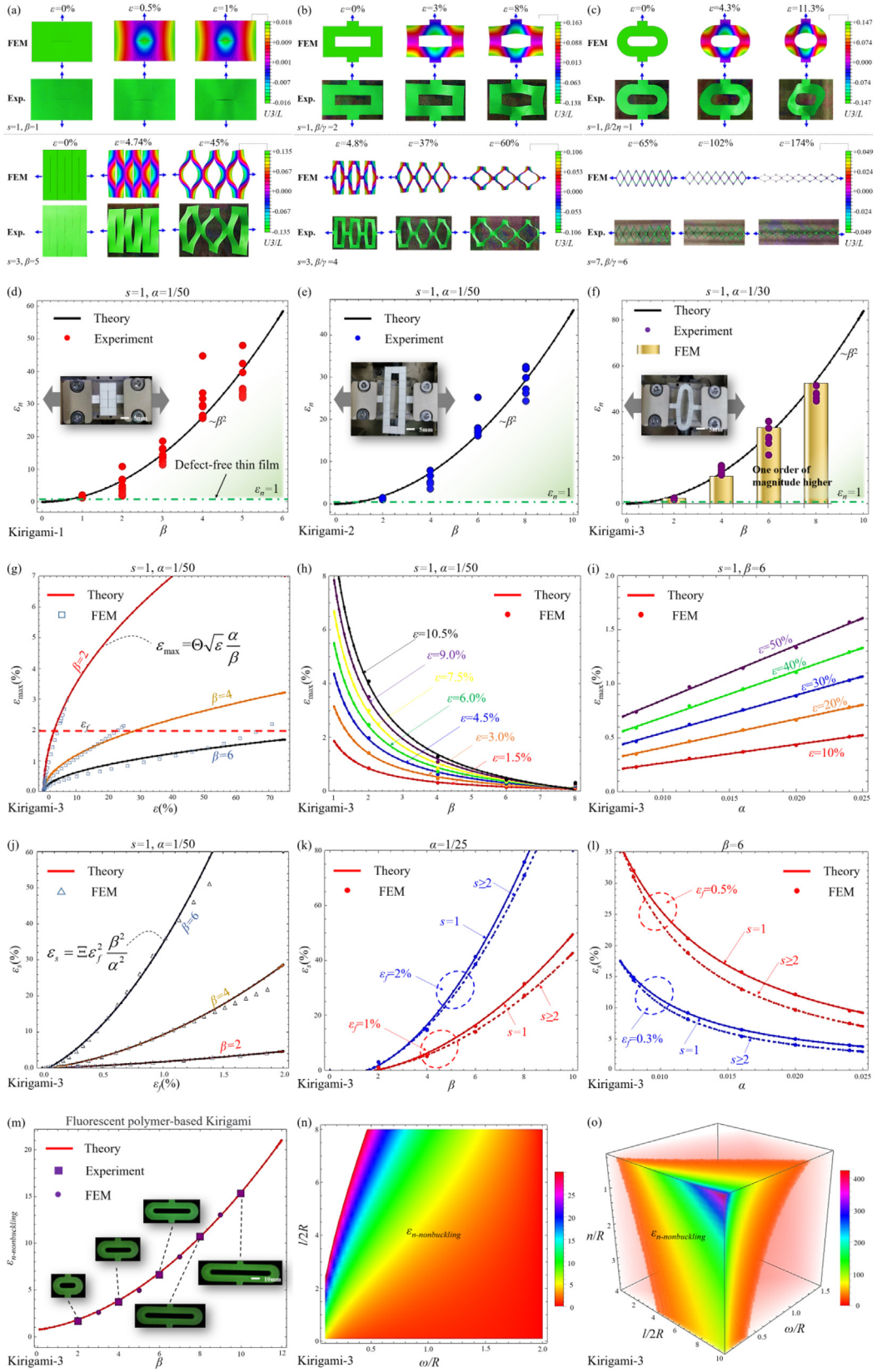

Fig. 4. (a–c) Numerical predictions of optical images of deformed configurations for Kirigami-1, Kirigami-2, and Kirigami-3, respectively. The color bars represent the out-of-plane displacement normalized by length L. (d–f) Normalized stretchability versus the geometric parameter β based on experimental, experimental, and FEM results for Kirigami-1, Kirigami-2, and Kirigami-3, respectively. (g–i) Scaling laws of the maximum tensile strain ε_{max}, which is proportional to (g) the square root of the applied strain ε, (h) the reciprocal of β, and (i) α. (j–l) Scaling laws of the elastic stretchability ε_s, which is proportional to (j) ε_f^2, (k) β^2, and (l) $1/\alpha^2$. (m–o) Scalability validation of the proposed theoretical framework using fluorescent polymer kirigami with large thickness via theories, experiments, and simulations: (m) elastic stretchability versus β; (n) distribution of the elastic stretchability with respect to the dimensionless parameters ω/R and $l/2R$; (o) distribution of $\varepsilon_{n-nonbuckling}$ with respect to the dimensionless parameters ω/R, $l/2R$, and n/R.

$$f_{n-2} = f_{n-2}(\beta, \gamma, \nu) \tag{9}$$

$$f_{n-3} = f_{n-3}(\beta, \eta, j(\eta), \nu) \tag{10}$$

where $j(\eta) = \eta - 1/\ln\left(\frac{2\eta+1}{2\eta-1}\right)$ in Eqs. (7) and (10) is associated with LCCB theory. The explicit forms of Eqs. (5)–(10) are given in SI Appendix, Note 3: see Eqs. (A16)–(A21). Fig. 2a–c show the geometry-dependent flexibility and normalized flexibility obtained using the closed-form analytical results from Eqs. (5)–(10). Over the whole domain, it is obvious that with decreasing kirigami thickness, the flexibility increases for given material properties and geometry. It can also be seen that both the flexibility and normalized flexibility increase monotonically with β (for the detailed functional relationships, see Eqs. (A16)–(A21)), i.e., a larger β will produce greater flexibility and normalized flexibility. More importantly, a significant long-arm effect plays an important role in enhancing the normalized flexibility by several orders of magnitude. For example, as shown in Fig. 2c, in the case of Kirigami-3 with geometric parameters $\beta = 10$ and $\gamma = 5$, the normalized flexibility is increased by 125 times compared with that of the defect-free thin film. These results are consistent with the experimental observations of ultrahigh flexibility of kirigami metastructures based on graphene (Blees et al., 2015), multifunctional kirigami composites (Shyu et al., 2015), kirigami polarization modulators (Choi et al., 2019), kirigami-inspired conducting nanosheets (Guan et al., 2018b), and programmable kiri-kirigami metamaterials (Tang et al., 2017) during initial in-plane deformation (Isobe and Okumura, 2016). The most important conclusion to be drawn from Fig. 2a–c is that not only do contour graphs give us more concrete results than closed-form analytical expressions but they do so for wider ranges of the geometric parameters, which suggests that enhancement of the normalized flexibility by more than several orders magnitude can be achieved by using simple kirigami designs instead of defect-free thin films.

The stress–strain curve presented in Fig. S1c (see stage *II* in SI Appendix, Note 1) also shows that kirigami metastructures (such as that with $\alpha = t/\omega = 1/50$) are characterized by a sudden transition from initially linear behavior to a plateau stress (Rafsanjani and Bertoldi, 2017). This results from out-of-plane buckling of straight beams in the kirigami. As the applied loading increases to a critical value, out-of-plane buckling occurs, and hinge behavior becomes energetically less costly than in-plane deformation (An et al., 2019; Rafsanjani and Bertoldi, 2017). From the energy approach (for details, see SI Appendix, Notes 4–6), it is found for the antisymmetric and symmetric buckling modes of the kirigami metastructures that the critical buckling forces can be written in the uniform form $F_{cr} = \left(\omega t^3\sqrt{EG}\right)/\chi l_j^2$, where χ is a function that depends on the boundary conditions, characteristic length, and buckling modes, and $l_j = \rho_j l$ is a characteristic length, which is related to the design variables ρ_j and the length l of the tailored vacancy. For example, in the case of the antisymmetric buckling mode for Kirigami-1, $\chi = \chi_1$ is equal to $3/\pi^3$ and $l_j = l_1 = l$ (for details, see SI Appendix, Note 4). By combining the stress–strain expressions for the prebuckling process (for details, see SI Appendix, Note 2) and the critical buckling forces, the following equations can be obtained, which can be solved to give the critical buckling strains ε_{cr-1}, ε_{cr-2}, and ε_{cr-3}:

$$\varepsilon_{cr-1} = \varepsilon_{cr-1}(\alpha, \beta, \chi_1(\beta), \nu) \tag{11}$$

$$\varepsilon_{cr-2} = \varepsilon_{cr-2}(\alpha, \beta, \gamma, \chi_2(\beta), \nu) \tag{12}$$

$$\varepsilon_{cr-3} = \varepsilon_{cr-3}(\alpha, \beta, \eta, j(\eta), \chi_3(\beta), \nu) \tag{13}$$

The explicit forms of Eqs. (11)–(13) are provided in SI Appendix, Note 7: see Eqs. (B23)–(B28).

The commercial FEM package Abaqus/standard is used to validate Eqs. (11)–(13) for various values of the geometric parameters α, β, γ, and η (for details, see SI Appendix, Note 13). The kirigami is assumed to be made of Kent paper, a high-quality paper with fine texture, used mainly for drafting (Isobe and Okumura, 2019). Fig. 3a–f show the effects of representative geometries on the critical buckling strain. Generally speaking, the FEM results are in excellent agreement with those obtained from the theoretical expressions for the critical buckling strain. Fig. 3a–c display the linear relationship, with the critical buckling strain being proportional to the square of the thickness-to-width ratio (i.e., α^2). In other words, with increasing α, the critical buckling strain increases, indicating that a larger value of α always hinders the onset of out-of-plane deformation for kirigami metastructures. The contribution of the thickness-to-width ratio to the critical buckling strain is consistent with previous experimental observations, such as those for hybrid kirigami metastructures (Hwang and Bartlett, 2018), geometry-dependent planar ribbon kirigami (Wang et al., 2020), kirigami-based wide-angle diffraction gratings (Xu et al., 2016), and high-performance stretchable heaters based on kirigami patterning (Jang et al., 2017). Moreover, preliminary inspection of Eqs. (11)–(13) suggests that their complexity makes it difficult to determine the effects of β, γ, and η on critical buckling strain. Therefore, we plot these expressions together with the results of FEM calculations in Fig. 3d–f. It can be seen that the ratio of critical buckling strain to α^2 decreases asβ (see Fig. 3a and d for Kirigami-1), β/γ (see Fig. 3b and e for Kirigami-2), and $\beta/2\eta$ (see Fig. 3c and f for Kirigami-3) increase. Also, for all cases shown in Fig. 3a–f, the ratio of critical buckling strain to α^2 varies less strongly when $\beta > 4$, $\beta/\gamma > 4$, and $\beta/2\eta > 4$. In particular, there is a less significant reduction of critical buckling strain due to increasing $\beta/2\eta$ in Kirigami-3. There is thus much evidence to indicate that the use of a kirigami design represents a desirable approach to regulating the onset of buckling (or critical buckling strain) in metastructures.

The critical buckling mode determines the subsequent deformation paths in the postbuckling regime (Zhang et al., 2013). From an examination of buckling modes through numerical simulations, it is apparent that the critical buckling mode with the minimum strain energy is strongly influenced by the geometric parameters β (see Fig. 3g for Kirigami-1), β/γ (see Fig. 3h for Kirigami-2), and $\beta/2\eta$ (see Fig. 3i for Kirigami-3), as well as by the number of unit cells s, whereas it is almost insensitive to the thickness-to-width ratio α (e.g., $\alpha = 1/50$) in the current study. To help provide a better understanding of the stability of kirigami metastructures, we present in Fig. 3g–i phase diagrams of critical buckling modes, obtained from numerical calculations. It can be seen that variations in buckling configurations are closely related to the antisymmetric mode and symmetric buckling mode as β (for Kirigami-1), β/γ (for Kirigami-2), $\beta/2\eta$ (for Kirigami-3), and s are varied. Obviously, the critical buckling modes are geometry-dependent. For example, in the case of Kirigami-3, the symmetric buckling mode occurs only when $s = 1$ (i.e., the kirigami metastructure has one unit cell) and $\beta/2\eta = 1$, whereas the antisymmetric buckling mode can occur when $s > 1$ and $\beta/2\eta > 1$ for all the other buckling cases. Fig. 3j–l present numerical snapshots of buckling modes for different geometries (different values of β, β/γ, $\beta/2\eta$, and s) at the critical buckling strain, with the color bars representing the out-of-plane displacement U_3. To better understand the geometric parameters controlling the buckling behaviors observed in numerical simulations, representative deformation patterns of Kirigami-3 can be directly demonstrated. For Kirigami-3 with $s = 1$ and $\beta/2\eta = 1$, the symmetric buckling mode occurs and corresponds to vertical displacement of the kirigami, while the out-of-plane displacement is symmetric about its transverse axis. The beam regions at the top

and bottom are partially deflected toward the out-of-plane direction, and the end regions of the kirigami undergo rigid body translation along the direction of external loading (for details, see Fig. 3l). For the case $\beta/2\eta > 1$ (e.g., $s = 2$ and $\beta/2\eta = 7$ in Fig. 3l), two sinusoidal beams in the unit cell can deform vertically up and down, and the out-of-plane displacement is antisymmetric about its transverse axis. The end regions at the top and bottom undergo a pair of antisymmetric out-of-plane displacements (shown in red and blue in the figure). As we demonstrated in Section 2, a kirigami in the antisymmetric configuration undergoes significant twisting and bending (for details, see Fig. 3l), and therefore deformation energy here results mainly from U_{B-A} induced by bending deformation, and U_{T-A} from torsional deformation. Based on these findings, it is noteworthy that an increase in the external loading cannot lead to qualitative variations in the pattern of out-of-plane deformation, but only to its accentuation. Therefore, in the next section, we investigate the postbuckling process and provide insights into the stretchability and normalized stretchability of kirigami metastructures.

4. Postbuckling response and stretchability

When the applied strain exceeds the critical buckling strain, kirigami metastructures can easily undergo out-of-plane buckling, since this consumes less energy than in-plane deformation. Here, we examine postbuckling responses closely connected with antisymmetric and symmetric buckling modes, and we develop scaling laws for the maximum tensile strain, elastic stretchability, and normalized stretchability. Fig. 4a–c compare experimental and numerical deformations associated with antisymmetric and symmetric buckling modes for a wide range of applied strain (e.g., up to 174% for Kirigami-3). The examples of kirigami metastructures in Fig. 4a–c were fabricated using laser cutting. Generally, the postbuckling responses from numerical calculations are consistent with experimental results. In particular, in the case of symmetrically deformed Kirigami-3 ($s = 1$ and $\beta/2\eta = 1$), the top and bottom beams both undergo combined bending and twisting deformations as the applied strain increases from 4.3% to 11.3% (see the experimental and numerical snapshots in Fig. 4c). In the case of antisymmetric kirigami, neighboring beams undergo antisymmetric deformations during the postbuckling process, as is evident in the snapshots of Kirigami-3 from 65% to 174% (see Fig. 4c, $s = 7$ and $\beta/2\eta = 6$). For significant deformation (e.g., with $\varepsilon > 174\%$), a distinct region of final stiffening (followed by rupture propagation) can be observed experimentally. This corresponds to a switch in the deformation mechanism from hinge behavior involving bending (and twisting) to stretching (An et al., 2019). Moreover, a similar response is visible in Fig. S1c (see stage *III* in SI Appendix, Note 1). These observations confirm the importance of developing a theoretical framework to describe the behavior of ultrastretchable kirigami with the aim of providing design guidelines for practical applications.

Here, we start by deriving a relationship between geometric parameters and the maximum tensile strain in kirigami metastructures, and we then present scaling laws for the elastic stretchability and normalized stretchability for Kirigami-1, Kirigami-2, and Kirigami-3. For a kirigami of rectangular cross section (e.g., with $t/\omega << 1$), the maximum tensile strain in the region of repeatable deformation, under the assumption of extreme points at the two ends of each kirigami beam, is given by the sum of the bending strains at the onset of buckling and at postbuckling:

$$\varepsilon_{\max} = \varepsilon_{cr} + \varepsilon_{post} = \frac{F_{cr} l \omega}{4EI_1} + \frac{t\left|\left(\Delta\kappa_y\right)_{\max}\right|}{2} \tag{14}$$

where $\left(\Delta\kappa_y\right)_{\max} = 4\pi^2\delta_{\max}/l^2$ (see SI Appendix, Note 5), $\delta_{\max} = Cl\sqrt{\varepsilon}$ (i.e., $\varepsilon \sim (\delta_{\max}/l)^2$, and C is the prefactor for Euler-type buckling), and $F_{cr} = \omega t^3\sqrt{EG}/\left(\chi l_j^2\right)$ (see SI Appendix, Note 6, Eq. (B20)). Therefore, the maximum tensile strain in the postbuckling kirigami can be expressed as

$$\varepsilon_{\max} = \frac{\alpha}{\beta}\left(\frac{3\sqrt{2}\alpha}{2\sqrt{1+\nu}\chi} + 2C\pi^2\sqrt{\varepsilon}\right) = \Theta\sqrt{\varepsilon}\frac{\alpha}{\beta} \tag{15}$$

where the strain at the onset of buckling is taken to be given by its approximation for $t/\omega << \varepsilon$ and it should be noted that Θ is geometry-dependent. Next, we define the normalized stretchability, which can be expressed as

$$\varepsilon_n = \frac{\varepsilon_s}{\varepsilon_f} = \frac{\varepsilon}{\varepsilon_{\max}} \tag{16}$$

where ε_s and ε_f are respectively the elastic stretchability and intrinsic failure strain of the material. The failure criterion for the kirigami that we use here is $\varepsilon_{\max} = \varepsilon_f$. For example, ε_f is the corresponding rupture strain for brittle materials. The combination of Eqs. (15) and (16) then gives the following expression for determining the elastic stretchability of the buckling kirigami:

$$\varepsilon_s = \Xi\varepsilon_f^2\frac{\beta^2}{\alpha^2} \tag{17}$$

where $\Xi = (1/\Theta)^2$. Inspection of Eq. (17) shows immediately that the relations between the elastic stretchability and the key geometric parameters are nonlinear and that $\partial\varepsilon_s/\partial\beta > 0$, $\partial\varepsilon_s/\partial\alpha < 0$, and $\partial\varepsilon_s/\partial\varepsilon_f > 0$, i.e., that ε_s increases with increasing β and ε_f, and with decreasing α.

Based on theoretical analysis, experiments, and FEM simulation, Fig. 4d–l illustrate the effects of geometric parameters (i.e., α, β, and s), applied strain ε, and intrinsic failure strain ε_f on the normalized stretchability ε_n, maximum tensile strain $\varepsilon_{\max}$ and elastic stretchability ε_s. Fig. 4d–f present comparisons of theoretical solutions, experimental results, and FEM simulations for the normalized stretchabilities of specific kirigami metastructures, namely, Kirigami-1, Kirigami-2, and Kirigami-3. In particular, in the case of Kirigami-3 with $s = 1$ and $\alpha = 1/30$ (Fig. 4f), the experimental and FEM results show good agreement with the theoretical solutions. The so-called long-arm effect can increase the normalized stretchability by as much as an order of magnitude, partially as a consequence of the low-level stress concentration on the arc. These results allow the first quantitative analysis of kirigami stretchability, and indicate that previous kirigami designs based solely on practical experience have not always been able to provide improved stretchability. However, some ultrastretchable devices have been constructed, such as metastructures based on kirigami conductors with 2000% stretchability (Guan et al., 2018b), ultrastretchable kirigami bioprobes (Morikawa et al., 2018), and kirigami actuators (Dias et al., 2017).

To explore the postbuckling properties in terms of the maximum tensile strain, Fig. 4g–i plot $\varepsilon_{\max}$ versus applied strain ε and the geometric parameters α and β for Kirigami-3. The curves in these three figures are all clearly monotonic, with the maximum tensile strain being proportional to the square root of the applied strain (see Fig. 4g), to the reciprocal of β (see Fig. 4h), and to α (see Fig. 4i). These results indicate that with a well-designed kirigami instead of a defect-free thin film, the maximum tensile strain can be substantially reduced, opening the way to a range of novel applications, including modulation of the stretchability of intrinsically brittle materials in extreme environments.

Fig. 4j–l reveal the dependence of the elastic stretchability on the intrinsic failure strain and on the geometric parameters. As can be seen from Fig. 4j, the elastic stretchability increases with

increasing intrinsic failure strain, with ε_s being proportional to ε_f^2. Fig. 4k and l respectively indicate that a larger β and a smaller α will generate greater elastic stretchability of ε_s. It is noteworthy, however, that the elastic stretchability is essentially independent of the number of unit cells for $s \geqslant 2$. Fig. 4k and l also show respectively that ε_s is proportional to β^2 and to $1/\alpha^2$, which is consistent with our experimental results.

In practical applications, novel physical devices based on kirigami metastructures require tunable deformations to maintain their performance. The above theoretical, experimental, and FEM results, taken together, allow straightforward optimization in the design of kirigami metastructures for successful application in ultrastretchable mechanical (Blees et al., 2015; Dias et al., 2017; Rafsanjani and Bertoldi, 2017; Zhao et al., 2018), electrical (Guan et al., 2018a, 2018b; Ma et al., 2018; Wang et al., 2017; Wu et al., 2016), and optical (Lamoureux et al., 2015; Tang et al., 2017; Xu et al., 2016) devices.

As a basis for further investigation and validation of the scalability of the proposed theoretical framework, we demonstrate the effects of geometry on the normalized stretchability $\varepsilon_{n-nonbuckling}$ for the fluorescent polymer-based Kirigami-3 with large thickness. All of our polymer-based kirigami metastructures are fabricated by 3D printing, and out-of-plane buckling is suppressed (the thickness-to-width ratio is equal to 10). In Fig. 4m–o, the results for $\varepsilon_{n-nonbuckling}$ from theoretical solutions, FEM calculations, and experiments (for details, see SI Appendix, Note 8) are plotted as a function of the dimensionless parameters β (Fig. 4m), ω/R and $l/2R$ (Fig. 4n), and ω/R and n/R (Fig. 4o). Larger values of β and $l/2R$, and smaller values of n/R and ω/R, lead to greater normalized stretchability. It is evident from Fig. 4m that the values of the normalized stretchability of the fluorescent polymer-based kirigami from experiments and FEM calculations are in surprisingly good agreement with the theoretical prediction, confirming that proposed theoretical framework using the energy approach and LCCB theory is highly effective and accurate in providing insights into the mechanically guided design of kirigami metastructures.

Finally, we note that many potential applications of buckling-induced kirigami are closely related to their out-of-plane mechanical properties. The out-of-plane stiffness varies as a function of the in-plane applied strain. As detailed in SI Appendix, Note 9, it is possible to make theoretical predictions of the out-of-plane stiffness of kirigami metastructures. The nonlinear normal force (Cao and Gao, 2019) stems from bending and pre-tension due to in-plane applied strain and nonlinear stretching effects (for details, see Eq. (C3) in SI Appendix, Note 9). For postbuckling kirigami, in the case of a small equivalent deflection, the out-of-plane stiffness can be expressed as a continuous function (for details, see Eq. (C9)). The remarkable postbuckling deformations of kirigami metastructures upon stretching can be partially explained in terms of the equivalent thickness and equivalent width using the standard deviation of the z and x coordinates (Wang et al., 2019). These hypotheses are confirmed by the numerical calculations, and the FEM results show good agreement with the theoretical solutions. It should be noted that the out-of-plane stiffness increases with increasing in-plane applied strain (for details, see Fig. S5b in SI Appendix, Note 9), which is in line with previous findings with regard to buckling-induced kirigami (Rafsanjani and Bertoldi, 2017).

5. Illustrative applications to mechanical programmability and energy harvesting

The results presented above should facilitate the development of programmable and functional devices that can simultaneously achieve ultrahigh flexibility and stretchability as well as steady device performance. Fig. 5 shows results for an ultrastretchable polyvinylidene fluoride (PVDF) kirigami integrated with a hybrid structural design, which holds promise for practical applications in energy harvesting. As a demonstration, we consider a specific programmable PVDF kirigami (Kirigami-3-hybrid) embedded in three different patterns/substructures (A, B, and C) with $\beta/2\eta = 2$, $\beta/2\eta = 3$, and $\beta/2\eta = 4$, respectively (i.e., the substructures A, B, and C can be characterized using the geometric parameters $\beta/2\eta = 2$, $\beta/2\eta = 3$, and $\beta/2\eta = 4$, respectively). To obtain the flexibility (for details, see SI Appendix, Note 10), we first revisit the stress–strain relation (for details, see SI Appendix, Note 2). Then, the combination of Eq. (A15) from SI Appendix, Note 2, $\varepsilon_H L = \frac{a}{s}\varepsilon_A L + \frac{b}{s}\varepsilon_B L + \frac{c}{s}\varepsilon_C L$ (according to Eq. (D4) from SI Appendix, Note 10)) and $\frac{\varepsilon_H}{f_H} = \frac{\varepsilon_A}{f_A} = \frac{\varepsilon_B}{f_B} = \frac{\varepsilon_C}{f_C}$ (according to Eq. (D5)) gives the following expression for the flexibility f_H of a programmable kirigami with hybrid structures:

$$f_H = \frac{af_A + bf_B + cf_C}{s} \tag{18}$$

where f_A, f_B, and f_C are the flexibilities of the respective substructures, and a, b, and c are the unit cell numbers corresponding to substructures A, B, and C, respectively. The following expressions for the critical buckling strain ε_{H-cr} and elastic stretchability ε_{H-s} of a programmable hybrid kirigami can be obtained in a similar manner:

$$\varepsilon_{H-cr} = \frac{a}{s}\varepsilon_{A-cr} + \frac{b}{s}\varepsilon_{B-cr} + \frac{c}{s}\varepsilon_{C-cr} \tag{19}$$

$$\varepsilon_{H-s} = \frac{a}{s}\varepsilon_{A-s} + \frac{b}{s}\varepsilon_{B-s} + \frac{c}{s}\varepsilon_{C-s} \tag{20}$$

where ε_{A-cr}, ε_{A-cr}, and ε_{C-cr} are the critical buckling strains of the respective substructures, and ε_{A-s}, ε_{B-s}, and ε_{C-s} are their elastic stretchabilities. Fig. 5a–c show the effects of a, b, and c on the flexibility f_H, critical buckling strain ε_{H-cr}, and elastic stretchability ε_{H-s}. In brief, for a hybrid kirigami metastructure with given unit cell numbers a and b, a larger value of c will generate larger ε_{H-s} and smaller ε_{H-cr}. Interestingly, a domino-like buckling effect occurred during our experimental observations (see Fig. 5f and, for details, SI Appendix, Note 11) and numerical calculations. In this effect, successive buckling of neighboring sections is triggered and leads to contraction of the kirigami. This happens because successive transitions of deformation energy in neighboring elements are sufficient to maintain a relatively stable energy level.

Based on these findings, a PVDF thin film with a cut pattern that is subject to a given applied strain can be designed. To understand the effect of electromechanical conversion, we examine the response of the normalized sensitivity $\bar{T}$ of the PVDF kirigami embedded into different geometries, with this response being captured using the partial derivative of the maximum output voltage $\Phi_{\max}$ under an open circuit with regard to the applied strain ε. Here, the normalized sensitivity $\bar{T}$ is given by

$$\bar{T} = \frac{\partial \Phi_{\max}}{\partial \varepsilon} \Big/ \left(\frac{d_{31}Et}{\left(e_{33} - Ed_{31}^2\right)} \right) \tag{21}$$

where d_{31} and e_{33} are the piezoelectric coefficient and dielectric constant, respectively. As can be seen from Fig. 5d (Kirigami-1), with increasing applied strain, the electric charge output is monotonically increasing, and our FEM calculations are in good agreement with the results of previous experiments (Hu et al., 2018). Fig. 5e shows the dependence of the normalized sensitivity on the applied strain for different samples of Kirigami-3 (with $\beta/2\eta = 3, 4, 5, 6$, respectively). The normalized sensitivity $\bar{T}$ remains almost unchanged during the entire process of stretching

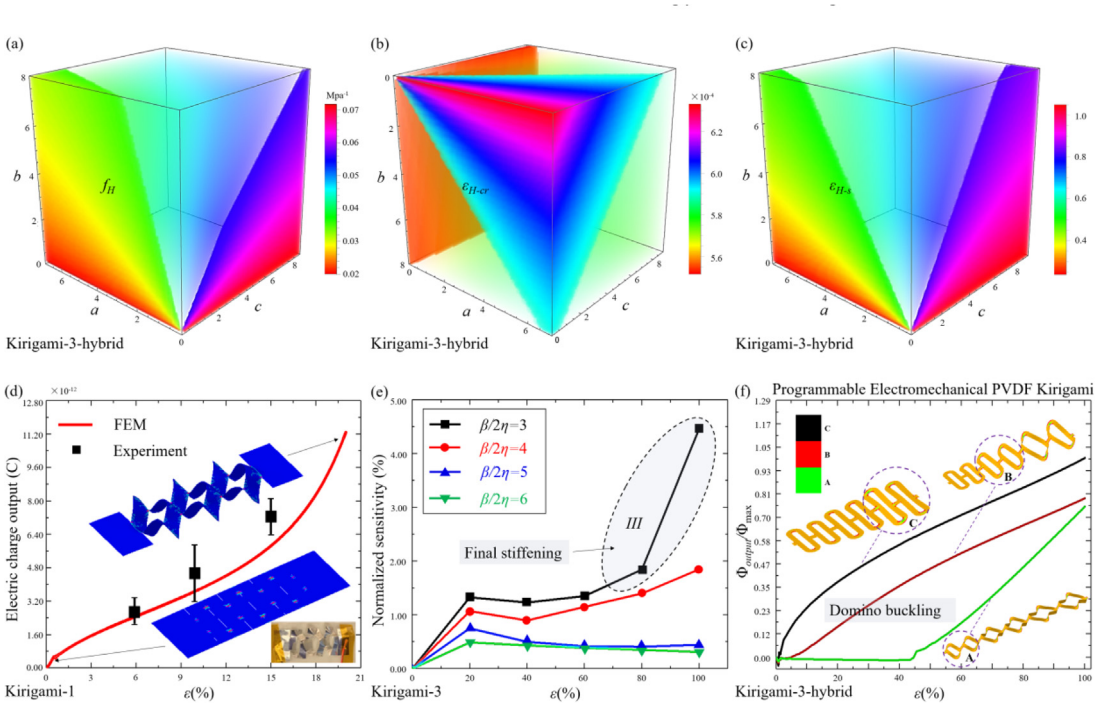

Fig. 5. (a–c) Distributions of flexibility, critical buckling strain, and elastic stretchability, respectively, with respect to substructure unit cell numbers *a*, *b*, and *c* in hybrid Kirigami-3. (d) Comparison of experimental (Hu et al., 2018) and FEM results for the electric charge output of PVDF Kirigami-1. (e) Effect of applied strain on normalized sensitivity for different geometries ($\beta/2\eta = 3$ to $\beta/2\eta = 6$), revealing how the final stiffening can significantly enhance the normalized sensitivity. (f) Normalized output voltage of a programmable electromechanical PVDF kirigami. The normalized output voltages for substructures A, B, and C are plotted using green, brown, and black lines. The domino-like buckling of the PVDF kirigami is also sketched (for details, see SI Appendix, Note 11). (For interpretation of the references to color in this figure legend, the reader is referred to the web version of this article.)

for large $\beta/2\eta$, i.e., $\beta/2\eta = 5$ and $\beta/2\eta = 6$. However, the effect of electromechanical conversion is amplified for smaller $\beta/2\eta$, such as $\beta/2\eta = 3$. This indicates that the final stiffening regime (see Fig. 5e and S1c (stage *III* in SI Appendix, Note 1)) can significantly enhance the normalized sensitivity of $\bar{T}$. Fig. 5f presents a design strategy for an electromechanical PVDF kirigami together with the normalized voltage output $\Phi_{output}/\Phi_{\max}$ versus the applied strain for substructures A, B, and C. It can be seen that the normalized output voltages for A, B, and C are distinctly different, which ensures the programmability of the electromechanical properties of the device. Moreover, unidirectional and fractal kirigami metamaterials have been developed based on rigid unit rotation (Fang et al., 2018; Tang et al., 2015). To obtain a better understanding of the electromechanical conversion effect, we consider the normalized sensitivities of kirigami metastructures and unidirectional and fractal kirigami metamaterials (see SI Appendix, Note 12). It has been found that these normalized sensitivities remain almost unchanged during the linear response and quasilinear response stages (Fang et al., 2018). In the third stage, the deformations of the three kirigami configurations are somewhat localized near the tips of the cuts, leading to hardening of the mechanical response, enhancement of the normalized sensitivity, and finally to rupture (Isobe and Okumura, 2016). It is noteworthy that the PVDF material we used here can be replaced by other functional materials that are widely used in biomedical devices, stretchable electronics, and energy harvesting.

6. Conclusions

The work presented here, through theoretical analysis, experiments, and FEM calculations, has, for the first time, provided a systematic description of prebuckling response, critical buckling strain, and postbuckling behavior of various kirigami metastructures. The highly accurate closed-form analytical solutions and scaling laws obtained provide insights into mechanically guided kirigami design. The excellent accuracy and scalability of the proposed theoretical framework have been comprehensively demonstrated using the energy approach, numerical simulations, and tensile experiments. Our study reveals that the remarkable long-arm effect can enhance the normalized flexibility and normalized stretchability by one or two orders of magnitude (by > 125 times and > 50 times, respectively). Theoretical, experimental, and numerical results reveal typical antisymmetric and symmetric buckling modes and the dimensionless geometric parameters α, β, γ, and η that control their onset. Details of the postbuckling deformations for both modes as well as their dependences on the maximum tensile strain and elastic stretchability have been uncovered via theoretical analyses, experiments and simulations. The out-of-plane stiffnesses of kirigami metastructures are found to be closely related to the buckling surface and in-plane applied strain. Based on these findings and a programmable design strategy, an ultrastretchable PVDF kirigami integrated with a hybrid structure can be constructed, which possesses stable electromechanical features associated with domino-like buckling effects. In summary, we have provided a theoretical basis for understanding the physics of buckling and thereby facilitating the development of ultrastretchable kirigami-based structures. The results obtained here expand the design space of kirigami structures and hold great promise for their application to programmable metastructures and metamaterials and to energy harvesting devices.

Declaration of Competing Interest

The authors declare that they have no known competing financial interests or personal relationships that could have appeared to influence the work reported in this paper.

Acknowledgments

This work was supported by National Natural Science Foundation of China, 11572099 and 11872160.

The author wishes to thank Mrs. Zaiying Zhang and Mr. Gongran Wang for their thoughtful kindness. The author wishes to thank Dr. Zeyi Zhang and Dr. Zihui Zhao for the technical supports.

The author would like to express his thanks to the editor and anonymous reviewers whose constructive comment significantly improved the paper.

Appendix A. Supplementary data

Supplementary data to this article can be found online at https://doi.org/10.1016/j.ijsolstr.2020.12.018.

References

An, N., Domel, A.G., Zhou, J., Rafsanjani, A., Bertoldi, K., 2019. Programmable hierarchical kirigami. Adv Funct. Mater., p. 1906711.

Babaee, S., Pajovic, S., Rafsanjani, A., Shi, Y., Bertoldi, K., Traverso, G. 2020. Bioinspired kirigami metasurfaces as assistive shoe grips. Nat. Biomed. Eng.

Bauer, J., Schroer, A., Schwaiger, R., Kraft, O., 2016. Approaching theoretical strength in glassy carbon nanolattices. Nat. Mater. 15, 438–443.

Berger, J.B., Wadley, H.N., McMeeking, R.M., 2017. Mechanical metamaterials at the theoretical limit of isotropic elastic stiffness. Nature 543, 533–537.

Blees, M.K., Barnard, A.W., Rose, P.A., Roberts, S.P., McGill, K.L., Huang, P.Y., Ruyack, A.R., Kevek, J.W., Kobrin, B., Muller, D.A., McEuen, P.L., 2015. Graphene kirigami. Nature 524, 204.

Callens, S.J.P., Zadpoor, A.A., 2018. From flat sheets to curved geometries: Origami and kirigami approaches. Mater. Today 21, 241–264.

Cao, G., Gao, H., 2019. Mechanical properties characterization of two-dimensional materials via nanoindentation experiments. Prog. Mater. Sci. 103, 558–595.

Chen, S.H., Chan, K.C., Yue, T.M., Wu, F.F., 2018. Highly stretchable kirigami metallic glass structures with ultra-small strain energy loss. Scripta Mater. 142, 83–87.

Choi, W.J., Cheng, G., Huang, Z., Zhang, S., Norris, T.B., Kotov, N.A., 2019. Terahertz circular dichroism spectroscopy of biomaterials enabled by kirigami polarization modulators. Nat. Mater. 18, 820–826.

Coulais, C., 2016. Periodic cellular materials with nonlinear elastic homogenized stress-strain response at small strains. Int. J. Solids Struct. 97–98, 226–238.

Dias, M.A., McCarron, M.P., Rayneau-Kirkhope, D., Hanakata, P.Z., Campbell, D.K., Park, H.S., Holmes, D.P., 2017. Kirigami actuators. Soft Matter 13, 9087–9092.

Fang, L., Li, J., Zhu, Z., Orrego, S., Kang, S.H., 2018. Piezoelectric polymer thin films with architected cuts. J. Mater. Res. 33, 330–342.

Florijn, B., Coulais, C., van Hecke, M., 2014. Programmable mechanical metamaterials. Phys. Rev. Lett. 113, 175503.

Guan, Y.S., Li, H., Ren, F., Ren, S., 2018a. kirigami-inspired conducting polymer thermoelectrics from electrostatic recognition driven assembly. ACS Nano 12, 7967–7973.

Guan, Y.S., Zhang, Z., Tang, Y., Yin, J., Ren, S., 2018b. Kirigami-inspired nanoconfined polymer conducting nanosheets with 2000% stretchability. Adv. Mater. 30, e1706390.

Hu, N., Chen, D., Wang, D., Huang, S., Trase, I., Grover, H.M., Yu, X., Zhang, J.X.J., Chen, Z. 2018. Stretchable Kirigami Polyvinylidene Difluoride Thin Films for Energy Harvesting: Design, Analysis, and Performance. Phys. Rev. Appl. 9.

Hwang, D.G., Bartlett, M.D., 2018. Tunable mechanical metamaterials through hybrid kirigami structures. Sci. Rep. 8, 3378.

Isobe, M., Okumura, K., 2016. Initial rigid response and softening transition of highly stretchable kirigami sheet materials. Sci. Rep. 6, 24758.

Isobe, M., Okumura, K. 2019. Continuity and discontinuity of kirigami's high-extensibility transition: A statistical-physics viewpoint. Phys. Rev. R. 1.

Jang, N.S., Kim, K.H., Ha, S.H., Jung, S.H., Lee, H.M., Kim, J.M., 2017. Simple approach to high-performance stretchable heaters based on kirigami patterning of conductive paper for wearable thermotherapy applications. ACS Appl. Mater. Inter. 9, 19612–19621.

Jin, S., Korkolis, Y.P., Li, Y., 2019. Shear resistance of an auxetic chiral mechanical metamaterial. Int. J. Solids Struct. 174–175, 28–37.

Lamoureux, A., Lee, K., Shlian, M., Forrest, S.R., Shtein, M., 2015. Dynamic kirigami structures for integrated solar tracking. Nat. Commun. 6, 8092.

Ma, R., Wu, C., Wang, Z.L., Tsukruk, V.V., 2018. Pop-up conducting large-area biographene kirigami. ACS Nano 12, 9714–9720.

Morikawa, Y., Yamagiwa, S., Sawahata, H., Numano, R., Koida, K., Ishida, M., Kawano, T. 2018. Ultrastretchable Kirigami Bioprobes. Adv. Healthc. Mater. 7.

Mortazavi, B., Lherbier, A., Fan, Z., Harju, A., Rabczuk, T., Charlier, J.C., 2017. Thermal and electronic transport characteristics of highly stretchable graphene kirigami. Nanoscale 9, 16329–16341.

Overvelde, J.T., Weaver, J.C., Hoberman, C., Bertoldi, K., 2017. Rational design of reconfigurable prismatic architected materials. Nature 541, 347–352.

Rafsanjani, A., Bertoldi, K., 2017. Buckling-induced kirigami. Phys. Rev. Lett. 118, 084301.

Rafsanjani, A., Jin, L., Deng, B., Bertoldi, K., 2019. Propagation of pop ups in kirigami shells. Proc. Natl. Acad. Sci. USA 116, 8200–8205.

Rafsanjani, A., Zhang, Y.R., Liu, B.Y., Rubinstein, S.M., Bertoldi, K. 2018. Kirigami skins make a simple soft actuator crawl. Sci. Robot. 3.

Shyu, T.C., Damasceno, P.F., Dodd, P.M., Lamoureux, A., Xu, L., Shlian, M., Shtein, M., Glotzer, S.C., Kotov, N.A., 2015. A kirigami approach to engineering elasticity in nanocomposites through patterned defects. Nat. Mater. 14, 785–789.

Tang, Y., Lin, G., Han, L., Qiu, S., Yang, S., Yin, J., 2015. Design of hierarchically cut hinges for highly stretchable and reconfigurable metamaterials with enhanced strength. Adv. Mater. 27, 7181–7190.

Tang, Y., Lin, G., Yang, S., Yi, Y.K., Kamien, R.D., Yin, J. 2017. Programmable Kiri-Kirigami Metamaterials. Adv. Mater. 29.

Wang, C., Wang, Y., 2018. The mechanical design of a hybrid intelligent hinge with shape memory polymer and spring sheet. Compos. Part B-Eng. 134, 1–8.

Wang, Y., Wang, C., 2020. Effect of temperature difference on the mechanical responses of ribbon kirigami: Toward the highly stretchable conductors. Int. J. Mech. Sci. 168.

Wang, Y., Wang, C., Tan, H., 2020. Geometry-dependent stretchability and stiffness of ribbon kirigami based on large curvature curved beam model. Int. J. Solids Struct. 182–183, 236–253.

Wang, Y., Wang, C., Zhang, Y., Guo, J., Tan, H. 2019. Dimensional variation of reconfigurable serpentine graphene nanoribbon under tension. J. Appl. Phys. 125.

Wang, Z., Zhang, L., Duan, S., Jiang, H., Shen, J., Li, C., 2017. Kirigami-patterned highly stretchable conductors from flexible carbon nanotube-embedded polymer films. J. Mater. Chem. C 5, 8714–8722.

Wu, C., Wang, X., Lin, L., Guo, H., Wang, Z.L., 2016. Paper-based triboelectric nanogenerators made of stretchable interlocking kirigami patterns. ACS Nano 10, 4652–4659.

Xu, L., Wang, X., Kim, Y., Shyu, T.C., Lyu, J., Kotov, N.A., 2016. Kirigami nanocomposites as wide-angle diffraction gratings. ACS Nano 10, 6156–6162.

Yang, Y., Dias, M.A., Holmes, D.P. 2018. Multistable kirigami for tunable architected materials. Phys. Rev. Mater. 2.

Zhang, Y., Xu, S., Fu, H., Lee, J., Su, J., Hwang, K.C., Rogers, J.A., Huang, Y., 2013. Buckling in serpentine microstructures and applications in elastomer-supported ultra-stretchable electronics with high areal coverage. Soft Matter 9, 8062–8070.

Zhang, Y., Zhang, F., Yan, Z., Ma, Q., Li, X., Huang, Y., Rogers, J.A., 2017. Printing, folding and assembly methods for forming 3D mesostructures in advanced materials. Nat. Rev. Mater. 2.

Zhao, R., Lin, S., Yuk, H., Zhao, X., 2018. Kirigami enhances film adhesion. Soft Matter 14, 2515–2525.

Zheng, X., Smith, W., Jackson, J., Moran, B., Cui, H., Chen, D., Ye, J., Fang, N., Rodriguez, N., Weisgraber, T., Spadaccini, C.M., 2016. Multiscale metallic metamaterials. Nat. Mater. 15, 1100–1106.